The University of Nottingham

UNITED KINGDOM · CHINA · MALAYSIA

Hartmann, Ralf and Houston, Paul (2005) Symmetric Interior Penalty DG Methods for the Compressible Navier-Stokes Equations II: Goal--Oriented A Posteriori Error Estimation.

SYMMETRIC INTERIOR PENALTY DG METHODS FOR THE COMPRESSIBLE NAVIER–STOKES EQUATIONS II: GOAL–ORIENTED A POSTERIORI ERROR ESTIMATION

RALF HARTMANN AND PAUL HOUSTON

Abstract. In this article we consider the application of the generalization of the symmetric version of the interior penalty discontinuous Galerkin finite element method to the numerical approximation of the compressible Navier–Stokes equations. In particular, we consider the a posteriori error analysis and adaptive mesh design for the underlying discretization method. Indeed, by employing a duality argument (weighted) Type I a posteriori bounds are derived for the estimation of the error measured in terms of general target functionals of the solution; these error estimates involve the product of the finite element residuals with local weighting terms involving the solution of a certain dual problem that must be numerically approximated. This general approach leads to the design of economical finite element meshes specifically tailored to the computation of the target functional of interest, as well as providing efficient error estimation. Numerical experiments demonstrating the performance of the proposed approach will be presented.

Key words. Discontinuous Galerkin methods, a posteriori error estimation, adaptivity, compressible Navier–Stokes equations

1. Introduction

In the recent series of articles [12, 13, 14, 17], we have been concerned with the development of so–called 'goal–oriented' a posteriori error estimation for h–version adaptive discontinuous Galerkin finite element methods (DGFEMs, for short) applied to inviscid compressible fluid flows; see also [19] and the references cited therein for the generalization to the hp–version of the DGFEM. Here, in contrast to traditional a posteriori error estimation which seeks to bound the error with respect to a given norm, goal–oriented a posteriori error estimation bounds the error measured in terms of certain output or target functionals of the solution of real or physical interest. Typical examples include the mean value of the field over the computational domain Ω, the normal flux through the outflow boundary of Ω, the evaluation of the solution at a given point in Ω and the drag and lift coefficients of a body immersed in a fluid. For related work, we refer to [6, 18], for example.

The purpose of this article is to extend our earlier work on nonlinear systems of first–order hyperbolic conservation laws to the compressible Navier–Stokes equations. As in the companion article [16], the discretization of the leading order terms is performed by employing the generalization of the symmetric version of the interior penalty DGFEM. One of the key aspects of this discretization scheme is the satisfaction of the adjoint consistency condition, cf. [1], for linear problems. This condition is essential to guarantee that the optimal order of convergence of the numerical approximation to the underlying analytical solution is attained when the discretization error is measured in terms of either the L_2–norm, or in the 'goal–oriented' setting, in terms of a given target functional of practical interest. By employing a duality argument we derive a weighted, or Type I, a posteriori error bound which reflects the error creation and error propagation mechanisms inherent

in viscous compressible fluid flows. On the basis of this a posteriori estimate, we design and implement the corresponding adaptive algorithm to ensure both the reliable and efficient control of the error in the prescribed target functional of interest. The superiority of the proposed approach over standard mesh refinement algorithms which employ (unweighted) empirical error indicators will be demonstrated. Additionally, we show numerically that the computed error representation formula can be employed to determine a improved value of the computed target functional $J(\cdot)$ of interest in order to yield a higher–order approximation to the exact value of this quantity.

The paper is structured as follows. After introducing, in Section 2, the compressible Navier–Stokes equations, in Section 3 we formulate its discontinuous Galerkin finite element approximation. Then, in Section 4 we derive an error representation formula together with the corresponding (weighted) Type I and (unweighted) Type II a posteriori error bounds for general target functionals of the solution. The error representation formula stems from a duality argument and includes computable residual terms multiplied by local weights involving the dual solution; the inclusion of the dual solution in the Type I bound ensures that the error creation and error propagation mechanisms inherent in viscous compressible fluid flows are reflected by the resulting local error indicators. On the basis of the (approximate) Type I error bound, in Section 5 we design and implement an adaptive algorithm that produces meshes specifically tailored to the efficient computation of the target functional of practical interest. The performance of the proposed adaptive strategy, and the quality of the (approximate) error representation formula and (approximate) Type I a posteriori bound, are then studied in Section 6 through a series of numerical experiments. Finally, in Section 7 we summarize the work presented in this paper and draw some conclusions.

The work presented in this paper is a complete and improved account of our recent work announced in the conference article [15].

2. Model Problem

Writing ρ, $\mathbf{v} = (v_1, v_2)^\top$, p, E, and T to denote the density, velocity vector, pressure, specific total energy, and temperature, respectively, the compressible Navier–Stokes equations are given by

$$(1) \qquad \nabla \cdot (\mathcal{F}^c(\mathbf{u}) - \mathcal{F}^v(\mathbf{u}, \nabla \mathbf{u})) \equiv \frac{\partial}{\partial x_i} \mathbf{f}_i^c(\mathbf{u}) - \frac{\partial}{\partial x_i} \mathbf{f}_i^v(\mathbf{u}, \nabla \mathbf{u}) = \mathbf{0} \quad \text{in } \Omega,$$

where Ω is an open bounded domain in $\mathbb{R}^2$. Here, and throughout the rest of this article, we use the summation convention, i.e., repeated indices are summed through their range. The vector of conservative variables $\mathbf{u}$, the convective fluxes $\mathbf{f}_i^c$, $i = 1, 2$, and the viscous fluxes $\mathbf{f}_i^v$, $i = 1, 2$, are defined by $\mathbf{u} = [\rho, \rho v_1, \rho v_2, \rho E]^\top$, $\mathbf{f}_i^c(\mathbf{u}) = [\rho v_i, \rho v_1 v_i + \delta_{1i} p, \rho v_2 v_i + \delta_{2i} p, \rho H v_i]^\top$, $i = 1, 2$, and $\mathbf{f}_i^v = [0, \tau_{1i}, \tau_{2i}, \tau_{i1} v_1 + \tau_{i2} v_2 + \mathcal{K} T_{x_i}]^\top$, $i = 1, 2$, respectively. Here, $\mathcal{K}$ is the thermal conductivity coefficient and H is the total enthalpy defined by $H = E + p/\rho$. The pressure is determined by the equation of state of an ideal gas, i.e.,

$$(2) \qquad\qquad p = (\gamma - 1)\rho(E - \tfrac{1}{2}\mathbf{v}^2),$$

where $\gamma = c_p/c_v$ is the ratio of specific heat capacities at constant pressure (c_p) and constant volume (c_v); for dry air, $\gamma = 1.4$. For a Newtonian fluid, the viscous

stress tensor is given by

$$(3) \qquad \tau = \mu \left(\nabla \mathbf{v} + (\nabla \mathbf{v})^\top - \tfrac{2}{3}(\nabla \cdot \mathbf{v}) I \right),$$

where μ is the dynamic viscosity coefficient; the temperature T is given by $\mathcal{K}T = \frac{\mu\gamma}{Pr}\left(E - \tfrac{1}{2}\mathbf{v}^2\right)$, where $\mathrm{Pr} = 0.72$ is the Prandtl number.

For the purposes of discretization, we rewrite the compressible Navier–Stokes equations (1) in the following (equivalent) form:

$$(4) \qquad \frac{\partial}{\partial x_i}\left(\mathbf{f}_i^c(\mathbf{u}) - G_{ij}(\mathbf{u})\frac{\partial \mathbf{u}}{\partial x_j}\right) = 0 \quad \text{in } \Omega.$$

Here, the matrices $G_{ij}(\mathbf{u}) = \partial \mathbf{f}_i^v(\mathbf{u}, \nabla \mathbf{u})/\partial \mathbf{u}_{x_j}$, for $i,j = 1,2$, i.e., $\mathbf{f}_i^v(\mathbf{u}, \nabla \mathbf{u}) = G_{ij}(\mathbf{u})\partial \mathbf{u}/\partial x_j$, $i = 1,2$, where

$$G_{11} = \frac{\mu}{\rho}\begin{pmatrix} 0 & 0 & 0 & 0 \\ -\tfrac{4}{3}v_1 & \tfrac{4}{3} & 0 & 0 \\ -v_2 & 0 & 1 & 0 \\ -\left(\tfrac{4}{3}v_1^2 + v_2^2 + \tfrac{\gamma}{Pr}\left(E - \mathbf{v}^2\right)\right) & \left(\tfrac{4}{3} - \tfrac{\gamma}{Pr}\right)v_1 & \left(1 - \tfrac{\gamma}{Pr}\right)v_2 & \tfrac{\gamma}{Pr} \end{pmatrix},$$

$$G_{12} = \frac{\mu}{\rho}\begin{pmatrix} 0 & 0 & 0 & 0 \\ \tfrac{2}{3}v_2 & 0 & -\tfrac{2}{3} & 0 \\ -v_1 & 1 & 0 & 0 \\ -\tfrac{1}{3}v_1 v_2 & v_2 & -\tfrac{2}{3}v_1 & 0 \end{pmatrix}, \quad G_{21} = \frac{\mu}{\rho}\begin{pmatrix} 0 & 0 & 0 & 0 \\ -v_2 & 0 & 1 & 0 \\ \tfrac{2}{3}v_1 & -\tfrac{2}{3} & 0 & 0 \\ -\tfrac{1}{3}v_1 v_2 & -\tfrac{2}{3}v_2 & v_1 & 0 \end{pmatrix},$$

$$G_{22} = \frac{\mu}{\rho}\begin{pmatrix} 0 & 0 & 0 & 0 \\ -v_1 & 1 & 0 & 0 \\ -\tfrac{4}{3}v_2 & 0 & \tfrac{4}{3} & 0 \\ -\left(v_1^2 + \tfrac{4}{3}v_2^2 + \tfrac{\gamma}{Pr}\left(E - \mathbf{v}^2\right)\right) & \left(1 - \tfrac{\gamma}{Pr}\right)v_1 & \left(\tfrac{4}{3} - \tfrac{\gamma}{Pr}\right)v_2 & \tfrac{\gamma}{Pr} \end{pmatrix}.$$

Given that $\Omega \subset \mathbb{R}^2$ is a bounded region, with boundary Γ, the system of conservation laws (4) must be supplemented by appropriate boundary conditions. As in [16], for simplicity of presentation, we assume that Γ may be decomposed as follows

$$\Gamma = \Gamma_{\mathrm{D,sup}} \cup \Gamma_{\mathrm{D,sub\text{-}in}} \cup \Gamma_{\mathrm{D,sub\text{-}out}} \cup \Gamma_{\mathrm{N}} \cup \Gamma_{\mathrm{W}},$$

where $\Gamma_{\mathrm{D,sup}}$, $\Gamma_{\mathrm{D,sub\text{-}in}}$, $\Gamma_{\mathrm{D,sub\text{-}out}}$, Γ_{N}, and Γ_{W} are distinct subsets of Γ representing Dirichlet (supersonic), Dirichlet (subsonic-inflow), Dirichlet (subsonic-outflow), Neumann (supersonic-outflow), and solid wall boundaries, respectively. Thereby, we may specify the following boundary conditions:

(5) $\mathcal{B}(\mathbf{u}) = \mathcal{B}(\mathbf{g}_D)$ on $\Gamma_{\mathrm{D,sup}} \cup \Gamma_{\mathrm{D,sub\text{-}in}} \cup \Gamma_{\mathrm{D,sub\text{-}out}}$, $\quad \mathcal{F}^v(\mathbf{u}, \nabla \mathbf{u}) \cdot \mathbf{n} = \mathbf{g}_{\mathrm{N}}$ on Γ_{N},

where $\mathbf{g}_{\mathrm{D}}$ and $\mathbf{g}_{\mathrm{N}}$ are given Dirichlet and Neumann boundary conditions, respectively. Here, $\mathcal{B}$ is a boundary operator employed to enforce appropriate Dirichlet conditions on $\Gamma_{\mathrm{D,sup}} \cup \Gamma_{\mathrm{D,sub\text{-}in}} \cup \Gamma_{\mathrm{D,sub\text{-}out}}$. For simplicity of presentation, we assume that $\mathcal{B}(\mathbf{u}) = \mathbf{u}$ on $\Gamma_{\mathrm{D,sup}}$, $\mathcal{B}(\mathbf{u}) = (u_1, u_2, u_3, 0)^\top$ on $\Gamma_{\mathrm{D,sub\text{-}in}}$, and $\mathcal{B}(\mathbf{u}) = \left(0, 0, 0, (\gamma - 1)(u_4 - (u_2^2 + u_3^2)/(2u_1))\right)^\top$ on $\Gamma_{\mathrm{D,sub\text{-}out}}$; we note that this latter condition enforces a specific pressure $p_{\mathrm{out}} = (\mathcal{B}(\mathbf{g_D}))_4$ on $\Gamma_{\mathrm{D,sub\text{-}out}}$.

For solid wall boundaries, we consider *isothermal* and *adiabatic* conditions; to this end, decomposing $\Gamma_W = \Gamma_{\mathrm{W,iso}} \cup \Gamma_{\mathrm{W,adia}}$, we set

$$\mathbf{v} = \mathbf{0} \ \text{ on } \ \Gamma_{\mathrm{W}}, \qquad T = T_{\mathrm{wall}} \ \text{ on } \ \Gamma_{\mathrm{W,iso}}, \qquad \mathbf{n} \cdot \nabla T = 0 \ \text{ on } \ \Gamma_{\mathrm{W,adia}},$$

where T_{wall} is a given wall temperature; see [4, 5, 7, 8, 9] and the references cited therein for further details

3. Discontinuous Galerkin Discretization

In this section we introduce the discontinuous Galerkin method with interior penalty for the discretization of the compressible Navier–Stokes equations (4); for full details concerning the derivation of the proposed scheme, we refer to the companion article [16].

We assume that Ω can be subdivided into shape-regular meshes $\mathcal{T}_h = \{\kappa\}$ consisting of quadrilateral elements κ. For each $\kappa \in \mathcal{T}_h$, we denote by $\mathbf{n}_\kappa$ the unit outward normal vector to the boundary $\partial\kappa$, and by h_κ the elemental diameter. An interior edge of $\mathcal{T}_h$ is the (non-empty) one-dimensional interior of $\partial\kappa^+ \cap \partial\kappa^-$, where κ^+ and κ^- are two adjacent elements of $\mathcal{T}_h$. Similarly, a boundary edge of $\mathcal{T}_h$ is the (non-empty) one-dimensional interior of $\partial\kappa \cap \Gamma$ which consists of entire edges of $\partial\kappa$. We denote by $\Gamma_\mathcal{I}$ the union of all interior edges of $\mathcal{T}_h$.

Next, we define average and jump operators. To this end, let κ^+ and κ^- be two adjacent elements of $\mathcal{T}_h$ and $\mathbf{x}$ be an arbitrary point on the interior edge $e = \partial\kappa^+ \cap \partial\kappa^- \subset \Gamma_\mathcal{I}$. Moreover, let $\mathbf{v}$ and $\underline{\tau}$ be vector- and matrix-valued functions, respectively, that are smooth inside each element $\kappa^\pm$. By $(\mathbf{v}^\pm, \underline{\tau}^\pm)$ we denote the traces of $(\mathbf{v}, \underline{\tau})$ on e taken from within the interior of $\kappa^\pm$, respectively. Then, we define the averages at $\mathbf{x} \in e$ by $\{\!\{\mathbf{v}\}\!\} = (\mathbf{v}^+ + \mathbf{v}^-)/2$ and $\{\!\{\underline{\tau}\}\!\} = (\underline{\tau}^+ + \underline{\tau}^-)/2$. Similarly, the jumps at $\mathbf{x} \in e$ are given by $[\![\mathbf{v}]\!] = \mathbf{v}^+ \otimes \mathbf{n}_{\kappa^+} + \mathbf{v}^- \otimes \mathbf{n}_{\kappa^-}$ and $[\![\underline{\tau}]\!] = \underline{\tau}^+ \cdot \mathbf{n}_{\kappa^+} + \underline{\tau}^- \cdot \mathbf{n}_{\kappa^-}$. For matrices $\underline{\sigma}, \underline{\tau} \in \mathbb{R}^{m \times n}$, $m, n \geq 1$, we use the standard notation $\underline{\sigma} : \underline{\tau} = \sum_{k=1}^m \sum_{l=1}^n \sigma_{kl} \tau_{kl}$; additionally, for vectors $\mathbf{v} \in \mathbb{R}^m, \mathbf{w} \in \mathbb{R}^n$, the matrix $\mathbf{v} \otimes \mathbf{w} \in \mathbb{R}^{m \times n}$ is defined by $(\mathbf{v} \otimes \mathbf{w})_{kl} = v_k w_l$.

Given a polynomial degree $p \geq 1$, we define the finite element space $\mathbf{V}_h = \{\mathbf{v} \in [L_2(\Omega)]^4 : \mathbf{v}|_\kappa \in [\mathcal{Q}_p(\kappa)]^4, \ \kappa \in \mathcal{T}_h\}$, where $\mathcal{Q}_p(\kappa)$ denotes the space of tensor product polynomials on κ of degree p in each coordinate direction. We consider the following interior penalty discontinuous Galerkin discretization of the compressible Navier–Stokes equations (4): find $\mathbf{u}_h \in \mathbf{V}_h$ such that

$$\mathcal{N}(\mathbf{u}_h, \mathbf{v}_h) \equiv -\int_\Omega \mathcal{F}^c(\mathbf{u}_h) : \nabla_h \mathbf{v}_h \, d\mathbf{x} + \sum_{\kappa \in \mathcal{T}_h} \int_{\partial\kappa \backslash \Gamma} \mathcal{H}(\mathbf{u}_h^+, \mathbf{u}_h^-, \mathbf{n}_\kappa) \cdot \mathbf{v}_h^+ \, ds$$

$$+ \int_\Omega \mathcal{F}^v(\mathbf{u}_h, \nabla_h \mathbf{u}_h) : \nabla_h \mathbf{v}_h \, d\mathbf{x} - \int_{\Gamma_\mathcal{I}} \{\!\{\mathcal{F}^v(\mathbf{u}_h, \nabla_h \mathbf{u}_h)\}\!\} : [\![\mathbf{v}_h]\!] \, ds$$

$$- \int_{\Gamma_\mathcal{I}} \{\!\{(G_{i1}^\top \partial_h \mathbf{v}_h / \partial x_i, G_{i2}^\top \partial_h \mathbf{v}_h / \partial x_i)\}\!\} : [\![\mathbf{u}_h]\!] \, ds + \int_{\Gamma_\mathcal{I}} \delta [\![\mathbf{u}_h]\!] : [\![\mathbf{v}_h]\!] \, ds$$

$$+ \int_\Gamma \mathcal{H}(\mathbf{u}_h^+, \mathbf{u}_\Gamma(\mathbf{u}_h^+), \mathbf{n}) \cdot \mathbf{v}_h^+ \, ds + \int_{\Gamma \backslash \Gamma_N} \delta \left(\mathbf{u}_h^+ - \mathbf{u}_\Gamma(\mathbf{u}_h^+) \right) \cdot \mathbf{v}_h^+ \, ds$$

$$- \int_{\Gamma \backslash (\Gamma_N \cup \Gamma_{W,\text{adia}})} \mathcal{F}^v(\mathbf{u}_h^+, \nabla_h \mathbf{u}_h^+) : [\![\mathbf{v}_h]\!] \, ds - \int_{\Gamma_N} \mathbf{g}_N \cdot \mathbf{v}_h \, ds$$

$$- \int_{\Gamma_{W,\text{adia}}} \mathcal{F}^{v,\text{adia}}(\mathbf{u}_h^+, \nabla_h \mathbf{u}_h^+) : [\![\mathbf{v}_h]\!] \, ds$$

$$(6) \quad - \int_{\Gamma \backslash \Gamma_N} \left(G_{i1}^\top(\mathbf{u}_h^+) \partial_h \mathbf{v}_h^+ / \partial x_i, G_{i2}^\top(\mathbf{u}_h^+) \partial_h \mathbf{v}_h^+ / \partial x_i \right) : \left(\mathbf{u}_h^+ - \mathbf{u}_\Gamma(\mathbf{u}_h^+) \right) \otimes \mathbf{n} \, ds = 0$$

for all $\mathbf{v}_h$ in $\mathbf{V}_h$. Here, the subscript h on the operators ∇_h and $\partial_h/\partial x_i$, $i = 1, 2$, is used to denote the discrete counterparts of ∇ and $\partial/\partial x_i$, $i = 1, 2$, respectively, defined elementwise. Furthermore, $\mathcal{H}(\cdot, \cdot, \cdot)$ denotes a *numerical (convective) flux*

function, assumed to be Lipschitz continuous, consistent and conservative. The discontinuity penalization matrix $\delta = \mathrm{diag}\{\delta_i, i = 1, \ldots, 4\}$ is set to

$$(7) \qquad \delta_i|_e = C_{\mathrm{IP}} \frac{\mu p^2}{\tilde{h}} \quad \text{for } e \subset \Gamma_{\mathcal{I}} \cup \Gamma,$$

where $\tilde{h} = \min(\mathrm{meas}(\kappa), \mathrm{meas}(\kappa'))/\mathrm{meas}(e)$ represents the element dimension orthogonal to the edge e of elements κ and κ' adjacent to e, and C_{IP} is a positive constant, which, for reasons of stability, must be chosen sufficiently large, cf. [1].

Finally, the boundary function $\mathbf{u}_\Gamma(\mathbf{u})$ is given according to the type of boundary condition imposed. To this end, we set $\mathbf{u}_\Gamma(\mathbf{u}) = \mathbf{g}_D$ on $\Gamma_{\mathrm{D,sup}}$, $\mathbf{u}_\Gamma(\mathbf{u}) = \mathbf{u}$ on Γ_{N}, $\mathbf{u}_\Gamma(\mathbf{u}) = ((g_D)_1, (g_D)_2, (g_D)_3, \frac{p(\mathbf{u})}{\gamma-1} + ((g_D)_2^2 + (g_D)_3^2)/(2(g_D)_1))^\top$ on $\Gamma_{\mathrm{D,sub\text{-}in}}$, and $\mathbf{u}_\Gamma(\mathbf{u}) = (u_1, u_2, u_3, \frac{p_{\mathrm{out}}}{\gamma-1} + (u_2^2 + u_3^2)/(2u_1))^\top$ on $\Gamma_{\mathrm{D,sub\text{-}out}}$. Here, $p \equiv p(\mathbf{u})$ denotes the pressure evaluated using the equation of state (2).

Finally, we set $\mathbf{u}_\Gamma(\mathbf{u}) = (u_1, 0, 0, u_1 c_v T_{\mathrm{wall}})^\top$ on $\Gamma_{\mathrm{W,iso}}$, $\mathbf{u}_\Gamma(\mathbf{u}) = (u_1, 0, 0, u_4)^\top$ on $\Gamma_{\mathrm{W,adia}}$, and define $\mathcal{F}^{v,\mathrm{adia}}(\mathbf{u}, \nabla \mathbf{u})$ such that

$$\mathcal{F}^{v,\mathrm{adia}}(\mathbf{u}, \nabla \mathbf{u}) \cdot \mathbf{n} = (0, \tau_{1j} n_{x_j}, \tau_{2j} n_{x_j}, \tau_{ij} v_j n_{x_i})^\top.$$

4. Goal–oriented a posteriori error estimation

In this section, we shall be concerned with controlling the error in the numerical approximation measured in terms of a given target functional $J(\cdot)$. Quantities of real or physical interest include the drag and lift coefficients, c_{d} and c_{l}, respectively, of a body immersed into a viscous fluid. These quantities are defined by

$$J_{c_{\mathrm{d}}}(\mathbf{u}) = J_{c_{\mathrm{dp}}}(\mathbf{u}) + J_{c_{\mathrm{df}}}(\mathbf{u}),$$
$$J_{c_{\mathrm{l}}}(\mathbf{u}) = J_{c_{\mathrm{lp}}}(\mathbf{u}) + J_{c_{\mathrm{lf}}}(\mathbf{u}),$$

respectively, where c_{dp} and c_{lp} are the pressure induced force coefficients given by

$$(8) \qquad J_{c_{\mathrm{dp}}}(\mathbf{u}) = \frac{2}{l\bar{\rho}|\bar{\mathbf{v}}|^2} \int_S p\,(\mathbf{n} \cdot \psi_d)\,\mathrm{d}s \quad \text{and} \quad J_{c_{\mathrm{lp}}}(\mathbf{u}) = \frac{2}{l\bar{\rho}|\bar{\mathbf{v}}|^2} \int_S p\,(\mathbf{n} \cdot \psi_l)\,\mathrm{d}s,$$

respectively, and c_{df} and c_{lf} are the viscous force coefficients, defined by

$$(9) \qquad J_{c_{\mathrm{df}}}(\mathbf{u}) = \frac{2}{l\bar{\rho}|\bar{\mathbf{v}}|^2} \int_S (\tau\,\mathbf{n}) \cdot \psi_d\,\mathrm{d}s \quad \text{and} \quad J_{c_{\mathrm{lf}}}(\mathbf{u}) = \frac{2}{l\bar{\rho}|\bar{\mathbf{v}}|^2} \int_S (\tau\,\mathbf{n}) \cdot \psi_l\,\mathrm{d}s,$$

respectively. Here, S denotes the surface of the body, l its chord length, $\bar{\mathbf{v}}$ and $\bar{\rho}$ are the reference (or free-stream) velocity and density, respectively, $(\tau\,\mathbf{n}) \cdot \psi = \tau_{ij} n_j \psi_i$, where τ is the viscous stress tensor defined in (3),

$$\psi_d = \begin{pmatrix} \cos(\alpha) & -\sin(\alpha) \\ \sin(\alpha) & \cos(\alpha) \end{pmatrix} \begin{pmatrix} 1 \\ 0 \end{pmatrix}, \qquad \psi_l = \begin{pmatrix} \cos(\alpha) & -\sin(\alpha) \\ \sin(\alpha) & \cos(\alpha) \end{pmatrix} \begin{pmatrix} 0 \\ 1 \end{pmatrix},$$

and α is the angle of attack. Other examples of $J(\cdot)$ include the local mean value of the field or its flux through the outflow boundary of the computational domain Ω, and the point evaluation of a component of $\mathbf{u}$ in Ω. For a more detailed discussion, we refer to the review articles [6, 19]. Assuming that $J(\cdot)$ is differentiable, we write

$$(10) \qquad \bar{J}(\mathbf{u}, \mathbf{u}_h; \mathbf{u} - \mathbf{u}_h) = J(\mathbf{u}) - J(\mathbf{u}_h) = \int_0^1 J'[\theta\mathbf{u} + (1-\theta)\mathbf{u}_h](\mathbf{u} - \mathbf{u}_h)\,\mathrm{d}\theta,$$

where $J'[\mathbf{w}](\cdot)$ denotes the Fréchet derivative of $J(\cdot)$ evaluated at some $\mathbf{w}$ in $\mathbf{V}$. Here, $\mathbf{V}$ is some suitably chosen function space such that $\mathbf{V}_h \subset \mathbf{V}$. Analogously,

we write

$$\mathcal{M}(\mathbf{u}, \mathbf{u}_h; \mathbf{u} - \mathbf{u}_h, \mathbf{v}) = \mathcal{N}(\mathbf{u}, \mathbf{v}) - \mathcal{N}(\mathbf{u}_h, \mathbf{v})$$

$$(11) \qquad\qquad = \int_0^1 \mathcal{N}'_{\mathbf{u}}[\theta \mathbf{u} + (1 - \theta) \mathbf{u}_h](\mathbf{u} - \mathbf{u}_h, \mathbf{v}) \, \mathrm{d}\theta$$

for all $\mathbf{v}$ in $\mathbf{V}$. Here, $\mathcal{N}'_{\mathbf{u}}[\mathbf{w}](\cdot, \mathbf{v})$ denotes the Fréchet derivative of $\mathbf{u} \mapsto \mathcal{N}(\mathbf{u}, \mathbf{v})$, for $\mathbf{v} \in \mathbf{V}$ fixed, at some $\mathbf{w}$ in $\mathbf{V}$. We remark that the linearization defined in (11) is only a *formal* calculation, in the sense that $\mathcal{N}'_{\mathbf{u}}[\mathbf{w}](\cdot, \cdot)$ may not in general exist. Instead, a suitable approximation to $\mathcal{N}'_{\mathbf{u}}[\mathbf{w}](\cdot, \cdot)$ must be determined, for example, by computing appropriate finite difference quotients of $\mathcal{N}(\cdot, \cdot)$, cf. [11, 12]. For the purposes of the current section, we assume that this linearization may be performed exactly; in Section 6 we employ the approximation to $\mathcal{N}'_{\mathbf{u}}[\mathbf{w}](\cdot, \cdot)$ defined in the companion article [16]. Given a suitable linearization, we introduce the following *dual* problem: find $\mathbf{z} \in \mathbf{V}$ such that

$$(12) \qquad\qquad \mathcal{M}(\mathbf{u}, \mathbf{u}_h; \mathbf{w}, \mathbf{z}) = \bar{J}(\mathbf{u}, \mathbf{u}_h; \mathbf{w}) \qquad \forall \mathbf{w} \in \mathbf{V}.$$

We assume that (12) possesses a unique solution. Clearly, the validity of this assumption depends on both the definition of $\mathcal{M}(\mathbf{u}, \mathbf{u}_h; \cdot, \cdot)$ and the choice of the target functional under consideration, cf. [12]. For the proceeding error analysis, we must therefore *assume* that the dual problem (12) is well–posed.

Proposition 4.1 (Error representation formula). *Let* $\mathbf{u}$ *and* $\mathbf{u}_h$ *denote the solutions of (4) and (6), respectively, and suppose that the dual problem (12) is well–posed. Then,*

$$(13) \qquad\qquad J(\mathbf{u}) - J(\mathbf{u}_h) = \mathcal{E}_\Omega(\mathbf{u}, \mathbf{u}_h; \mathbf{z} - \mathbf{z}_h) \equiv \sum_{\kappa \in \mathcal{T}_h} \eta_\kappa,$$

where

$$\eta_\kappa = \int_\kappa \mathbf{R}(\mathbf{u}_h) \cdot \boldsymbol{\omega}_\hbar \, d\mathbf{x} + \int_{\partial\kappa \backslash \Gamma} (\mathcal{F}^c(\mathbf{u}_h) \cdot \mathbf{n}_\kappa - \mathcal{H}(\mathbf{u}_h^+, \mathbf{u}_h^-, \mathbf{n}_\kappa)) \cdot \boldsymbol{\omega}_\hbar^+ \, ds$$

$$+ \int_{\partial\kappa \cap \Gamma} (\mathcal{F}^c(\mathbf{u}_h) \cdot \mathbf{n}_\kappa - \mathcal{H}(\mathbf{u}_h^+, \mathbf{u}_\Gamma(\mathbf{u}_h^+), \mathbf{n}_\kappa)) \cdot \boldsymbol{\omega}_\hbar^+ \, ds$$

$$+ \frac{1}{2} \int_{\partial\kappa \backslash \Gamma} \left((G_{i1}^\top \partial_h \boldsymbol{\omega}_\hbar / \partial x_i, G_{i2}^\top \partial_h \boldsymbol{\omega}_\hbar / \partial x_i) : \llbracket \underline{\mathbf{u}_h} \rrbracket - \llbracket \mathcal{F}^v(\mathbf{u}_h, \nabla \mathbf{u}_h) \rrbracket \cdot \boldsymbol{\omega}_\hbar^+ \right) ds$$

$$- \int_{\partial\kappa \backslash \Gamma} \delta \llbracket \underline{\mathbf{u}_h} \rrbracket : \boldsymbol{\omega}_\hbar^+ \otimes \mathbf{n}_\kappa \, ds - \int_{\partial\kappa \cap (\Gamma \backslash \Gamma_N)} \delta \left(\mathbf{u}_h^+ - \mathbf{u}_\Gamma(\mathbf{u}_h^+) \right) \cdot \boldsymbol{\omega}_\hbar^+ \, ds$$

$$- \int_{\partial\kappa \cap \Gamma_N} (\mathcal{F}^v(\mathbf{u}_h^+, \nabla \mathbf{u}_h^+) \cdot \mathbf{n}_\kappa - \mathbf{g}_N) \cdot \boldsymbol{\omega}_\hbar^+ \, ds$$

$$- \int_{\partial\kappa \cap \Gamma_{W,adia}} \left(\mathcal{F}^v(\mathbf{u}_h^+, \nabla \mathbf{u}_h^+) - \mathcal{F}^{v,adia}(\mathbf{u}_h^+, \nabla \mathbf{u}_h^+) \right) : \boldsymbol{\omega}_\hbar^+ \otimes \mathbf{n} \, ds$$

$$+ \int_{\partial\kappa \cap (\Gamma \backslash \Gamma_N)} \left(G_{i1}^\top(\mathbf{u}_h^+) \partial_h \boldsymbol{\omega}_\hbar^+ / \partial x_i, G_{i2}^\top(\mathbf{u}_h^+) \partial_h \boldsymbol{\omega}_\hbar^+ / \partial x_i \right) : \left(\mathbf{u}_h^+ - \mathbf{u}_\Gamma(\mathbf{u}_h^+) \right) \otimes \mathbf{n} \, ds,$$

and $\boldsymbol{\omega}_\hbar = \mathbf{z} - \mathbf{z}_h$ *for all* $\mathbf{z}_h$ *in* $\mathbf{V}_h$*. Here,* $\mathbf{R}(\mathbf{u}_h)|_\kappa = -\nabla \cdot \mathcal{F}^c(\mathbf{u}_h) + \nabla \cdot \mathcal{F}^v(\mathbf{u}_h, \nabla \mathbf{u}_h)$*,* $\kappa \in \mathcal{T}_h$*, denotes the elementwise residual.*

Proof. Choosing $\mathbf{w} = \mathbf{u} - \mathbf{u}_h$ in (12), recalling the linearization performed in (10), and exploiting the Galerkin orthogonality property of the DGFEM, we get

$$
\begin{aligned}
J(\mathbf{u}) - J(\mathbf{u}_h) &= \bar{J}(\mathbf{u}, \mathbf{u}_h; \mathbf{u} - \mathbf{u}_h) = \mathcal{M}(\mathbf{u}, \mathbf{u}_h; \mathbf{u} - \mathbf{u}_h, \mathbf{z}) \\
&= \mathcal{M}(\mathbf{u}, \mathbf{u}_h; \mathbf{u} - \mathbf{u}_h, \mathbf{z} - \mathbf{z}_h) = -\mathcal{N}(\mathbf{u}_h, \mathbf{z} - \mathbf{z}_h) \ \forall \mathbf{z}_h \in \mathbf{V}_h.
\end{aligned}
$$

Equation (13) now follows by application of the divergence theorem. $\qquad\square$

Remark 4.2. *We note that the dependence of the error representation formula $\mathcal{E}_{\Omega}(\mathbf{u}, \mathbf{u}_h; \mathbf{z} - \mathbf{z}_h)$ on the unknown analytical solution $\mathbf{u}$ to the compressible Navier–Stokes equations (4) stems from the linearizations performed in (10) and (11).*

From the error representation formula (13) we can easily derive the following Type I error bound.

Corollary 4.3 (Type I error bound)**.** *Given that the assumptions of Proposition 4.1 hold. Then,*

$$
\tag{14} J(\mathbf{u}) - J(\mathbf{u}_h) \le \sum_{\kappa \in \mathcal{T}_h} \eta_{\kappa}^{(\mathrm{I})},
$$

where $\eta_{\kappa}^{(\mathrm{I})} = |\eta_{\kappa}|$, and η_{κ} as given in Proposition 4.1.

Proof. Equation (14) follows from (13) by employing the triangle inequality. $\qquad\square$

We now proceed to derive a so–called unweighted, or Type II, a posteriori error bound, where the dependence of the dual solution $\mathbf{z}$ only enters the resulting estimate via a stability constant. To this end, under the foregoing assumption that the underlying computational meshes employed, $\mathcal{T}_h$, parameterised by $h > 0$, are shape-regular, we first recall the following approximation result; cf. [3], for example.

Lemma 4.4. *Given $\kappa \in \mathcal{T}_h$, suppose that $v|_{\kappa} \in H^{k_{\kappa}}(\kappa), 0 \le k_{\kappa} \le p+1$. Then, there exists Πv in $\mathcal{Q}_p(\kappa)$, a constant C_{int} dependent on k_{κ}, p, and the shape-regularity of $\mathcal{T}_h$, but independent of v and h_{κ}, such that for $0 \le q \le k_{\kappa}$,*

$$
\tag{15} \|v - \Pi v\|_{H^q(\kappa)} \le C_{\mathrm{int}} h_{\kappa}^{k_{\kappa} - q} \|v\|_{H^{k_{\kappa}}(\kappa)}.
$$

Moreover, by employing Lemma 4.4, together with the multiplicative trace inequality

$$
\|v\|_{L_2(\partial\kappa)} \le C_{\mathrm{trace}} \left(\|v\|_{L_2(\kappa)} \|\nabla v\|_{L_2(\kappa)} + h_{\kappa}^{-1} \|v\|_{L_2(\kappa)}^2 \right)^{1/2},
$$

where $C_{\mathrm{trace}} > 0$ is a constant, dependent solely on the shape-regularity of $\mathcal{T}_h$, we deduce that, given $v|_{\kappa} \in H^{k_{\kappa}}(\kappa)$ for some $1 \le k_{\kappa} \le p+1$ and $\kappa \in \mathcal{T}_h$,

$$
\tag{16} \|v - \Pi v\|_{L_2(\partial\kappa)} \le C h_{\kappa}^{k_{\kappa} - 1/2} \|v\|_{H^{k_{\kappa}}(\kappa)}.
$$

Similarly, given $v|_{\kappa} \in H^{k_{\kappa}}(\kappa)$ for some $2 \le k_{\kappa} \le p+1$ and $\kappa \in \mathcal{T}_h$, we have

$$
\tag{17} \|v - \Pi v\|_{H^1(\partial\kappa)} \le C h_{\kappa}^{k_{\kappa} - 3/2} \|v\|_{H^{k_{\kappa}}(\kappa)}.
$$

In (16) and (17), C is a positive constant, different at each occurrence, which depends on the shape-regularity of $\mathcal{T}_h$ and the polynomial degree p, but is independent of the mesh size.

Equipped with (15), (16), and (17), we now prove the following Type II a posteriori error bound.

Corollary 4.5 (Type II error bound). *Given that the assumptions of Proposition 4.1 hold, suppose that $\mathbf{z} \in [H^s(\Omega)]^4$, $2 \leq s \leq p+1$, and that we have found a constant C_{stab} such that*

$$(18) \qquad\qquad \|\mathbf{z}\|_{H^s(\Omega)} \leq C_{\mathrm{stab}}.$$

Then, the following Type II *a posteriori error bound holds:*

$$(19) \qquad\qquad |J(\mathbf{u}) - J(\mathbf{u}_h)| \leq C \left(\sum_{\kappa \in \mathcal{T}_h} \left(\eta_\kappa^{(\mathrm{II})} \right)^2 \right)^{1/2},$$

where

$$
\begin{aligned}
\eta_\kappa^{(\mathrm{II})} =\ & \|h_\kappa^s \mathbf{R}(\mathbf{u}_h)\|_{L_2(\kappa)} + \|h_\kappa^{s-1/2}(\mathcal{F}^c(\mathbf{u}_h) \cdot \mathbf{n}_\kappa - \mathcal{H}(\mathbf{u}_h^+, \mathbf{u}_h^-, \mathbf{n}_\kappa))\|_{L_2(\partial\kappa \backslash \Gamma)} \\
& + \|h_\kappa^{s-1/2}(\mathcal{F}^c(\mathbf{u}_h) \cdot \mathbf{n}_\kappa - \mathcal{H}(\mathbf{u}_h^+, \mathbf{u}_\Gamma(\mathbf{u}_h^+), \mathbf{n}_\kappa))\|_{L_2(\partial\kappa \cap \Gamma)} \\
& + \|h_\kappa^{s-3/2} G_{\cdot j} \underline{[\![\mathbf{u}_h]\!]}_j\|_{L_2(\partial\kappa \backslash \Gamma)} + \|h_\kappa^{s-1/2} [\![\mathcal{F}^v(\mathbf{u}_h, \nabla\mathbf{u}_h)]\!]\|_{L_2(\partial\kappa \backslash \Gamma)} \\
(20) \quad & + \|h_\kappa^{s-1/2} \delta \left(\mathbf{u}_h^+ - \mathbf{u}_h^- \right)\|_{L_2(\partial\kappa \backslash \Gamma)} \\
& + \|h_\kappa^{s-1/2} \delta \left(\mathbf{u}_h^+ - \mathbf{u}_\Gamma(\mathbf{u}_h^+) \right)\|_{L_2(\partial\kappa \cap (\Gamma \backslash \Gamma_N))} \\
& + \|h_\kappa^{s-1/2}(\mathcal{F}^v(\mathbf{u}_h^+, \nabla\mathbf{u}_h^+) \cdot \mathbf{n}_\kappa - \mathbf{g}_N)\|_{L_2(\partial\kappa \cap \Gamma_N)} \\
& + \|h_\kappa^{s-1/2} \left(\mathcal{F}^v(\mathbf{u}_h^+, \nabla\mathbf{u}_h^+) - \mathcal{F}^{v,adia}(\mathbf{u}_h^+, \nabla\mathbf{u}_h^+) \right) \cdot \mathbf{n}_\kappa\|_{L_2(\partial\kappa \cap \Gamma_{W,adia})} \\
& + \|h_\kappa^{s-3/2} G_{\cdot j}(\mathbf{u}_h^+) \left[(\mathbf{u}_h^+ - \mathbf{u}_\Gamma(\mathbf{u}_h^+)) \otimes \mathbf{n} \right]_j\|_{L_2(\partial\kappa \cap (\Gamma \backslash \Gamma_N))}
\end{aligned}
$$

and C *is a positive constant depending on the shape-regularity of the mesh, the polynomial degree and the regularity of the dual solution, but is independent of the mesh size. For interior edges, we have used the notation*

$$
\|G_{\cdot j} \underline{[\![\mathbf{u}_h]\!]}_j\|_{L_2(\partial\kappa)} = \left(\sum_{i=1}^2 \int_{\partial\kappa} \left| G_{ij} \underline{[\![\mathbf{u}_h]\!]}_j \right|^2 ds \right)^{\frac{1}{2}},
$$

where for a $m \times n$ matrix A, we write A_j, $1 \leq j \leq n$, to denote the m–vector consisting of the jth column of A; the last term on the right-hand side of (20) is also defined in an analogous manner.

Proof. Selecting $\mathbf{z}_h = \Pi\mathbf{z}$, applying the Cauchy–Schwarz inequality, together with the approximation results (15), (16), and (17), we note that the local error indicator $|\eta_\kappa|$, cf. Proposition 4.1, may be bounded as follows:

$$
\begin{aligned}
|\eta_\kappa| \leq\ & C \Big(\|h_\kappa^s \mathbf{R}(\mathbf{u}_h)\|_{L_2(\kappa)} + \|h_\kappa^{s-1/2}(\mathcal{F}^c(\mathbf{u}_h) \cdot \mathbf{n}_\kappa - \mathcal{H}(\mathbf{u}_h^+, \mathbf{u}_h^-, \mathbf{n}_\kappa))\|_{L_2(\partial\kappa \backslash \Gamma)} \\
& + \|h_\kappa^{s-1/2}(\mathcal{F}^c(\mathbf{u}_h) \cdot \mathbf{n}_\kappa - \mathcal{H}(\mathbf{u}_h^+, \mathbf{u}_\Gamma(\mathbf{u}_h^+), \mathbf{n}_\kappa))\|_{L_2(\partial\kappa \cap \Gamma)} \\
& + \|h_\kappa^{s-3/2} G_{\cdot j} \underline{[\![\mathbf{u}_h]\!]}_j\|_{L_2(\partial\kappa \backslash \Gamma)} + \|h_\kappa^{s-1/2} [\![\mathcal{F}^v(\mathbf{u}_h, \nabla\mathbf{u}_h)]\!]\|_{L_2(\partial\kappa \backslash \Gamma)} \\
& + \|h_\kappa^{s-1/2} \delta \left(\mathbf{u}_h^+ - \mathbf{u}_h^- \right)\|_{L_2(\partial\kappa \backslash \Gamma)} \\
& + \|h_\kappa^{s-1/2} \delta \left(\mathbf{u}_h^+ - \mathbf{u}_\Gamma(\mathbf{u}_h^+) \right)\|_{L_2(\partial\kappa \cap (\Gamma \backslash \Gamma_N))} \\
& + \|h_\kappa^{s-1/2}(\mathcal{F}^v(\mathbf{u}_h^+, \nabla\mathbf{u}_h^+) \cdot \mathbf{n}_\kappa - \mathbf{g}_N)\|_{L_2(\partial\kappa \cap \Gamma_N)} \\
& + \|h_\kappa^{s-1/2} \left(\mathcal{F}^v(\mathbf{u}_h^+, \nabla\mathbf{u}_h^+) - \mathcal{F}^{v,\mathrm{adia}}(\mathbf{u}_h^+, \nabla\mathbf{u}_h^+) \right) \cdot \mathbf{n}_\kappa\|_{L_2(\partial\kappa \cap \Gamma_{W,\mathrm{adia}})} \\
(21) \quad & + \|h_\kappa^{s-3/2} G_{\cdot j}(\mathbf{u}_h^+) \left[(\mathbf{u}_h^+ - \mathbf{u}_\Gamma(\mathbf{u}_h^+)) \otimes \mathbf{n} \right]_j\|_{L_2(\partial\kappa \cap (\Gamma \backslash \Gamma_N))} \Big) \|\mathbf{z}\|_{H^s(\kappa)},
\end{aligned}
$$

for $2 \leq s \leq p+1$, where C is a positive constant which depends on the shape-regularity of the mesh $\mathcal{T}_h$ and the polynomial degree, but is independent of the mesh size. Here, for the fourth and tenth terms on the right–hand side of (21), we have employed the following identity:

$$\left(G_{i1}^\top \partial_h \boldsymbol{\omega}_\hbar / \partial x_i, G_{i2}^\top \partial_h \boldsymbol{\omega}_\hbar / \partial x_i\right) : [\![\mathbf{u}_h]\!] = G_{ij} [\![\mathbf{u}_h]\!]_j \cdot \partial_h \boldsymbol{\omega}_\hbar / \partial x_i.$$

Upon summing over the elements in the mesh $\mathcal{T}_h$, application of the Cauchy–Schwarz inequality, together with the stability bound (18), the statement of the corollary follows immediately. □

We note that the error representation formula (13) and the Type I a posteriori error bound (14) depends on the unknown analytical solution to the primal and dual problems, $\mathbf{u}$ and $\mathbf{z}$, respectively. Thus, in order to render these quantities computable, both $\mathbf{u}$ and $\mathbf{z}$ must be replaced by suitable approximations. Here, the linearizations leading to $\mathcal{M}(\mathbf{u}, \mathbf{u}_h; \cdot, \cdot)$ and $\bar{J}(\mathbf{u}, \mathbf{u}_h; \cdot)$ are performed about $\mathbf{u}_h$ and the dual solution $\mathbf{z}$ is replaced by a DGFEM approximation $\hat{\mathbf{z}}$ computed on the same mesh $\mathcal{T}_h$ used for $\mathbf{u}_h$, but with a higher degree polynomial.

Notwithstanding these approximations, we shall show through numerical experimentation in Section 6, that the reliability of the Type I a posteriori error bound (14) is not compromised, in the sense that $\sum_{\kappa \in \mathcal{T}_h} \hat{\eta}_\kappa^{(\mathrm{I})}$, where $\hat{\eta}_\kappa^{(\mathrm{I})} = |\hat{\eta}_\kappa|$ and $\hat{\eta}_\kappa$ is defined in an analogous manner to η_κ, cf. Proposition 4.1, with $\mathbf{z}$ replaced by $\hat{\mathbf{z}}$, remains an upper bound on the true error in the target functional $J(\cdot)$. Furthermore, we shall show that the ratio of the approximate error representation formula

$$(22) \qquad \mathcal{E}_\Omega(\mathbf{u}_h, \mathbf{u}_h; \hat{\mathbf{z}} - \mathbf{z}_h) \equiv \sum_{\kappa \in \mathcal{T}_h} \hat{\eta}_\kappa$$

and the true value $J(\mathbf{u}) - J(\mathbf{u}_h)$ is extremely close to one; see [10, 12, 13, 18], for related work.

Before we end this section, we finally note that provided the linearization error is *sufficiently* small and the analytical solutions to the underlying compressible Navier–Stokes equations and the corresponding dual problem are *sufficiently* regular, then the approximate error representation formula (22) may be used to improve the computed value of the target functional of interest, $J(\mathbf{u}_h)$. To see this, we note that the error representation formula may be written as follows:

$$\begin{aligned} J(\mathbf{u}) - J(\mathbf{u}_h) &= \mathcal{E}_\Omega(\mathbf{u}_h, \mathbf{u}_h; \hat{\mathbf{z}} - \mathbf{z}_h) + \mathcal{E}_\Omega(\mathbf{u}_h, \mathbf{u}_h; \mathbf{z} - \hat{\mathbf{z}}) \\ (23) \qquad &\quad + \mathcal{E}_\Omega(\mathbf{u}, \mathbf{u}_h; \mathbf{z} - \mathbf{z}_h) - \mathcal{E}_\Omega(\mathbf{u}_h, \mathbf{u}_h; \mathbf{z} - \mathbf{z}_h). \end{aligned}$$

Here, the first term on the right–hand side of (23) is the approximate error representation formula which is actually computed in practice, cf. above. Given that $\hat{\mathbf{z}}$ is computed using higher–order polynomials to those employed for $\mathbf{u}_h$, the second term on the right–hand side of (23) will be of higher–order than the first, provided that the dual solution is sufficiently regular. The last two terms on the right–hand side of (23) represent the error incurred through linearization; in cases when the analytical solution $\mathbf{u}$ is smooth, we would expect these terms to be relatively small. Thereby, in these circumstances, we can expect that the modified value of the target functional, namely,

$$\tilde{J}(\mathbf{u}_h) = J(\mathbf{u}_h) + \mathcal{E}_\Omega(\mathbf{u}_h, \mathbf{u}_h; \hat{\mathbf{z}} - \mathbf{z}_h)$$

should provide an improved estimate of the actual value of the target functional $J(\mathbf{u})$; this will be demonstrated numerically in Section 6.

5. Adaptive mesh refinement

In this section we consider the design of an adaptive algorithm to ensure the efficient computation of the given target functional $J(\cdot)$ of practical interest. To this end, we employ the approximate Type I a posteriori error bound $\sum_{\kappa \in \mathcal{T}_h} \hat{\eta}_\kappa^{(\mathrm{I})}$ to determine when the desired level of accuracy has been achieved. For example, suppose that the aim of the computation is to compute $J(\cdot)$ such that the error $|J(\mathbf{u}) - J(\mathbf{u}_h)|$ is less than some user-defined tolerance TOL, i.e.,

$$|J(\mathbf{u}) - J(\mathbf{u}_h)| \leq \mathtt{TOL};$$

then, in practice we may enforce the stopping criterion

$$\sum_{\kappa \in \mathcal{T}_h} \hat{\eta}_\kappa^{(\mathrm{I})} \leq \mathtt{TOL}.$$

If this condition is not satisfied on the current finite element mesh $\mathcal{T}_h$, then the elementwise terms $\hat{\eta}_\kappa^{(\mathrm{I})}$ are employed as local error indicators to guide mesh refinement and coarsening. The cycle of the adaptive mesh refinement is outlined as follows:

(1) Construct an initial mesh $\mathcal{T}_h$.
(2) Compute $\mathbf{u}_h \in \mathbf{V}_h$ on the current mesh $\mathcal{T}_h$.
(3) Compute $\hat{\mathbf{z}} \in \hat{\mathbf{V}}_h$, where $\hat{\mathbf{V}}_h$ is a finite element space defined in an analogous manner to $\mathbf{V}_h$ based on the (same) computational mesh $\mathcal{T}_h$, but consisting of piecewise (discontinuous) polynomials of degree $\hat{p} > p$.
(4) Evaluate the approximate a posteriori error bound $\sum_{\kappa \in \mathcal{T}_h} \hat{\eta}_\kappa^{(\mathrm{I})}$.
(5) If $\sum_{\kappa \in \mathcal{T}_h} \hat{\eta}_\kappa^{(\mathrm{I})} \leq \mathtt{TOL}$, where TOL is a given tolerance, then STOP.
(6) Otherwise, refine and coarsen a fixed fraction of the total number of elements according to the size of $\hat{\eta}_\kappa^{(\mathrm{I})}$ and generate a new mesh $\mathcal{T}_h$; GOTO 2.

6. Numerical experiments

In this section we present a series of numerical examples to highlight the advantages of designing an adaptive finite element algorithm based on the weighted error indicator $\hat{\eta}_\kappa^{(\mathrm{I})}$, in comparison to an adaptive algorithm based on an empirical (unweighted) refinement indicator which does not require the solution of an auxiliary (dual) problem; for simplicity, we employ the Type II residual–based indicator $\eta_\kappa^{(\mathrm{II})}$ defined in Section 4. Throughout this section, we employ the Vijayasundaram flux for the discretization of the convective terms and set $p = 1$ (bilinear elements). As in [16], we select the constant C_{IP} appearing in the discontinuity penalisation parameter δ_i, $i = 1, \ldots, 4$, defined in (7) as follows: $C_{\mathrm{IP}} = 10$. Finally, for both adaptive refinement strategies, we use the fixed fraction refinement algorithm with refinement and derefinement fractions set to 20% and 10%, respectively; we also note that for the computation of $\hat{\eta}_\kappa^{(\mathrm{I})}$, the dual solution is approximated using piecewise biquadratic polynomials, i.e., $\hat{p} = 2$.

6.1. Mach 0.5 flow at Re = 5000 and $\alpha = 0°$ around a NACA0012. In this example, we consider the subsonic viscous flow around a NACA0012 airfoil; here, the upper and lower surfaces of the airfoil geometry are specified by the function $g^\pm$, respectively, where

$$g^\pm(s) = \pm 5 \times 0.12 \times (0.2969 s^{1/2} - 0.126 s - 0.3516 s^2 + 0.2843 s^3 - 0.1015 s^4).$$
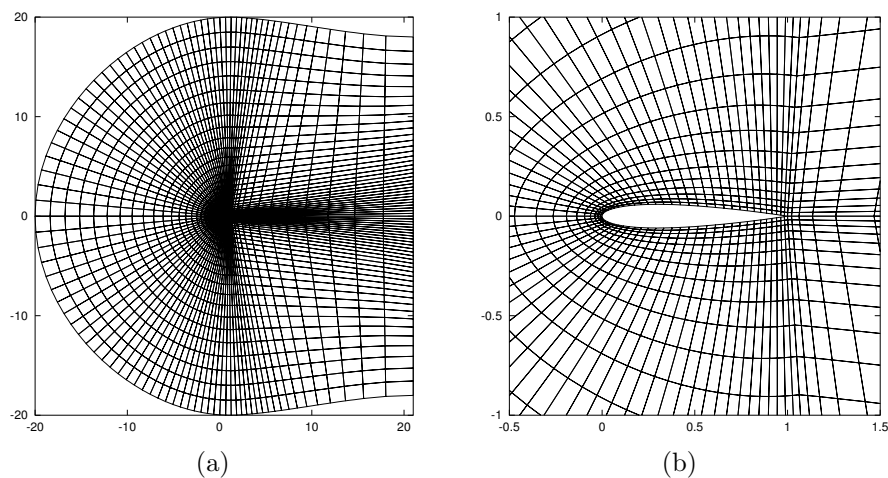
FIGURE 1. Computational mesh with 3072 elements: (a) Full view; (b) Zoom of the mesh.
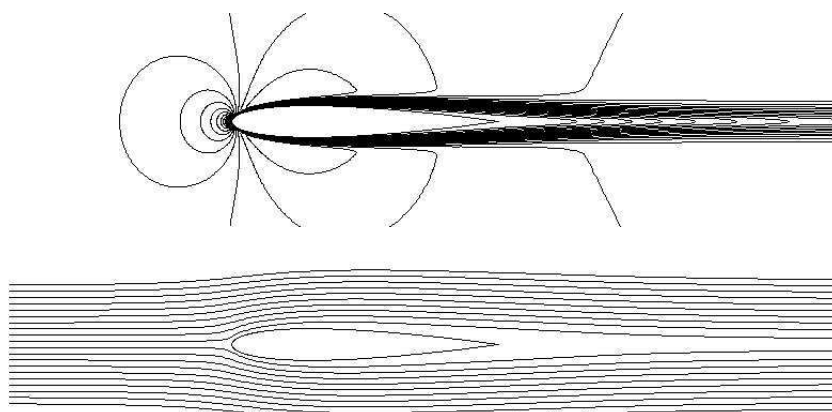

FIGURE 2. $M = 0.5, \mathrm{Re} = 5000, \alpha = 0°$ flow around the NACA0012 airfoil: (top) Mach isolines; (bottom) Streamlines.

As the chord length l of the airfoil is $l \approx 1.00893$ we use a rescaling of g in order to yield an airfoil of unit (chord) length. The computational domain Ω is subdivided into quadrilateral elements; cf. the C-type mesh depicted in Figure 1. Curved boundaries are approximated by piecewise quadratic polynomials. At the farfield (inflow) boundary we specify a Mach 0.5 flow at a zero angle of attack, i.e. $\alpha = 0°$, with Reynolds number $\mathrm{Re} = 5000$; on the walls of the airfoil geometry, we impose a zero heat flux (adiabatic) no-slip boundary condition. This is a standard laminar test case which has been investigated by many other authors, cf. [5], for example; this test case was also considered in the companion–article [16] in order to demonstrate the convergence of the inviscid and viscous drag coefficients, c_{dp} and c_{df}, respectively, on the surface of the airfoil under both global and local mesh

TABLE 1. $M = 0.5, \mathrm{Re} = 5000, \alpha = 0°$ flow around the NACA0012 airfoil: Adaptive algorithm for the numerical approximation of c_{dp} based on employing the Type I error indicator $\hat{\eta}_\kappa^{(\mathrm{I})}$.

Elements	DoF	$J(\mathbf{u}) - J(\mathbf{u}_h)$	$\sum_{\kappa \in \mathcal{T}_h} \hat{\eta}_\kappa$	θ_1	$\sum_{\kappa \in \mathcal{T}_h} |\hat{\eta}_\kappa|$	θ_2
3072	49152	1.522e-02	1.040e-02	0.68	1.963e-02	1.29
4929	78864	4.410e-03	3.839e-03	0.87	6.659e-03	1.51
8097	129552	1.262e-03	1.156e-03	0.92	2.208e-03	1.75
13467	215472	3.285e-04	3.106e-04	0.95	7.156e-04	2.18
21846	349536	8.918e-05	8.675e-05	0.97	2.725e-04	3.06
35610	569760	2.536e-05	2.530e-05	1.00	1.253e-04	4.94

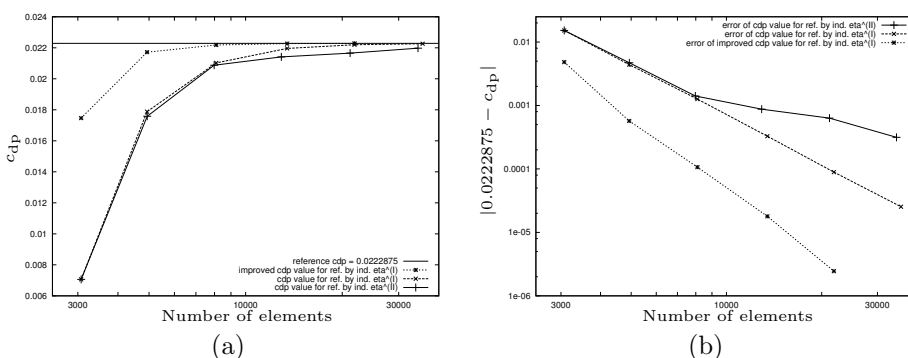(a)   (b)

FIGURE 3. $M = 0.5, \mathrm{Re} = 5000, \alpha = 0°$ flow around the NACA0012 airfoil: (a) Computed values of c_{dp} based on employing the error indicators $\hat{\eta}_\kappa^{(\mathrm{I})}$ and $\eta_\kappa^{(\mathrm{II})}$, together with the improved value; (b) Convergence of the error in these quantities.

refinement. The solution to this problem consists of a strictly subsonic flow which is symmetric about the x-axis, see Figure 2. On the basis of a fine grid computation, the reference values for these quantities of interest are given by $J_{c_{\mathrm{dp}}}(\mathbf{u}) \approx 0.0222875$ and $J_{c_{\mathrm{df}}}(\mathbf{u}) \approx 0.032535$.

In Table 1 we demonstrate the performance of the adaptive algorithm for the numerical approximation of the inviscid drag coefficient, i.e. when $J(\cdot) \equiv J_{c_{\mathrm{dp}}}(\cdot)$, based on employing the weighted Type I error indicators $\hat{\eta}_\kappa^{(\mathrm{I})}$. Here, we show the number of elements and degrees of freedom (DoF) in $\mathbf{V}_h$, the true error in the functional $J(\mathbf{u}) - J(\mathbf{u}_h)$, the computed error representation formula, the approximate a posteriori error bound, and their respective effectivity indices $\theta_1 = \sum_{\kappa \in \mathcal{T}_h} \hat{\eta}_\kappa / (J(\mathbf{u}) - J(\mathbf{u}_h))$ and $\theta_2 = \sum_{\kappa \in \mathcal{T}_h} |\hat{\eta}_\kappa| / |J(\mathbf{u}) - J(\mathbf{u}_h)|$; here, we recall that $\hat{\eta}_\kappa^{(\mathrm{I})} = |\hat{\eta}_\kappa|$. We see that initially on very coarse meshes the quality of the computed error representation formula $\sum_{\kappa \in \mathcal{T}_h} \hat{\eta}_\kappa$ is rather poor, in the sense that θ_1 noticeably differs from one; however, as the mesh is refined, we observe that the effectivity indices θ_1 slowly tend towards unity. On the other hand, just the application of the triangle inequality leads to reliable error estimation, even on the

TABLE 2. $M = 0.5, \mathrm{Re} = 5000, \alpha = 0°$ flow around the NACA0012 airfoil: Adaptive algorithm for the numerical approximation of c_{df} based on employing the Type I error indicator $\hat{\eta}_\kappa^{(\mathrm{I})}$.

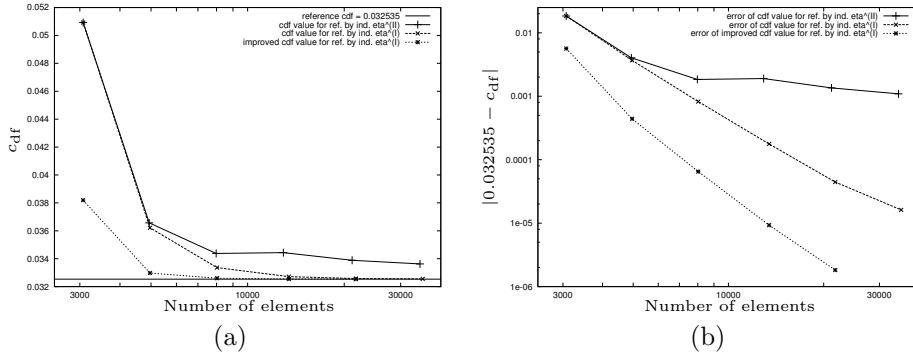| Elements	DoF	$J(\mathbf{u}) - J(\mathbf{u}_h)$	$\sum_{\kappa \in \mathcal{T}_h} \hat{\eta}_\kappa$	θ_1	$\sum_{\kappa \in \mathcal{T}_h} |\hat{\eta}_\kappa|$	θ_2
3072	49152	-1.839e-02	-1.274e-02	0.69	2.430e-02	1.32
4962	79392	-3.680e-03	-3.239e-03	0.88	9.399e-03	2.55
8028	128448	-8.246e-04	-7.596e-04	0.92	4.209e-03	5.10
13446	215136	-1.773e-04	-1.680e-04	0.95	2.067e-03	11.65
21750	348000	-4.444e-05	-4.258e-05	0.96	1.044e-03	23.48
35118	561888	-1.624e-05	-1.626e-05	1.00	5.328e-04	32.82

(a)   (b)

FIGURE 4. $M = 0.5, \mathrm{Re} = 5000, \alpha = 0°$ flow around the NACA0012 airfoil: (a) Computed values of c_{df} based on employing the error indicators $\hat{\eta}_\kappa^{(\mathrm{I})}$ and $\eta_\kappa^{(\mathrm{II})}$, together with the improved value; (b) Convergence of the error in these quantities.

coarsest mesh; indeed, here we see that θ_2 is always greater than one, though we do observe a slight increase in this quantity as the mesh is refined.

In Figure 3 we compare the true error in the computed target functional $J_{c_{\mathrm{dp}}}(\cdot)$ using the two mesh refinement strategies. Here, we clearly observe the superiority of employing the weighted Type I a posteriori error indicator; on the final mesh, the true error in the computed target functional is over an order of magnitude smaller than $|J_{c_{\mathrm{dp}}}(\mathbf{u}) - J_{c_{\mathrm{dp}}}(\mathbf{u}_h)|$ computed on the sequence of meshes produced using $\eta_\kappa^{(\mathrm{II})}$. Moreover, here we also show the error in the improved value of the inviscid drag coefficient, i.e. $|J_{c_{\mathrm{dp}}}(\mathbf{u}) - \tilde{J}_{c_{\mathrm{dp}}}(\mathbf{u}_h)|$; in this case, we clearly see that this error is of higher–order than the baseline error $|J_{c_{\mathrm{dp}}}(\mathbf{u}) - J_{c_{\mathrm{dp}}}(\mathbf{u}_h)|$. Indeed, on the finest mesh the error in the improved target functional is over an order of magnitude smaller than the corresponding quantity computed with the weighted Type I error indicator. We also point out that after just one mesh refinement step, the improved value $\tilde{J}_{c_{\mathrm{dp}}}(\mathbf{u}_h)$ computed on the mesh refined using the weighted Type I indicator is more accurate than the corresponding value $J_{c_{\mathrm{dp}}}(\mathbf{u}_h)$ computed on the *finest* mesh designed on the basis of employing the Type II error indicator.
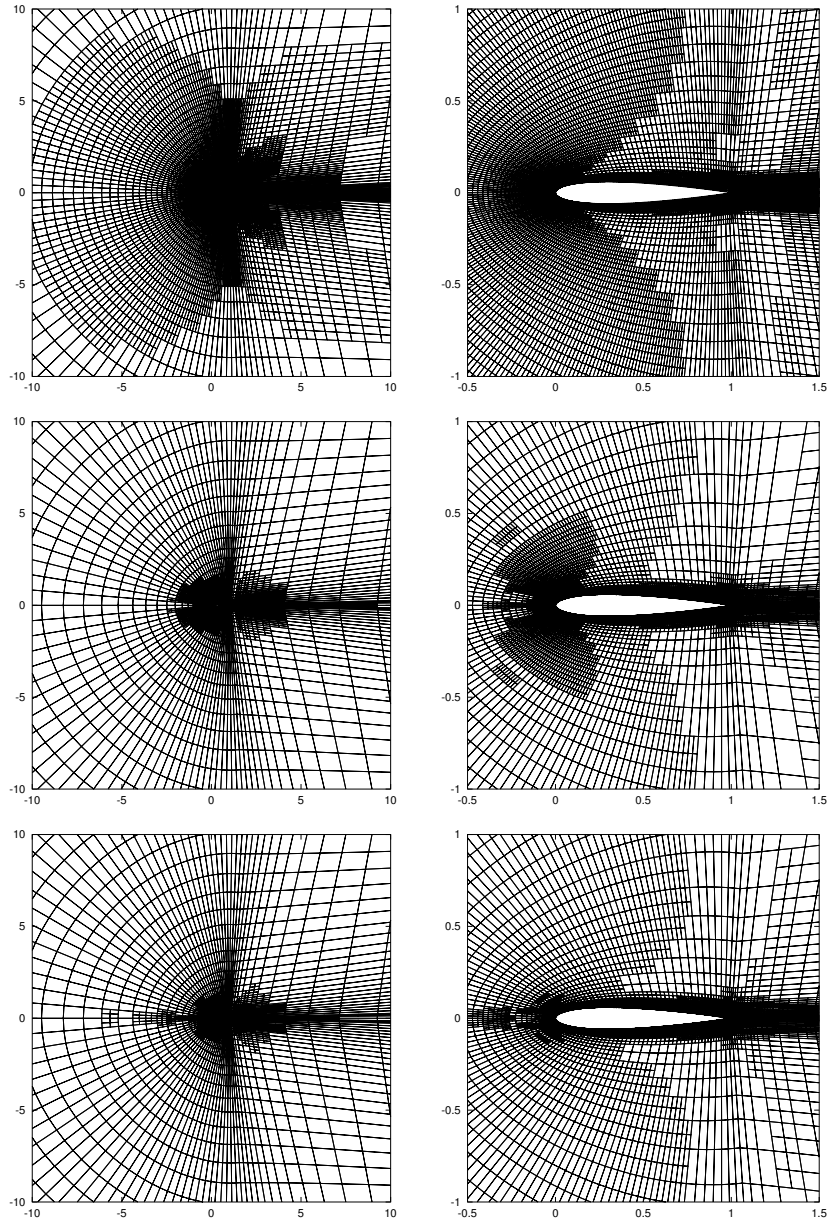
FIGURE 5. $M = 0.5, \mathrm{Re} = 5000, \alpha = 0°$ flow around the NACA0012 airfoil: Meshes constructed using (top row) Type II error indicators; (middle row) Weighted Type I error indicators for c_{dp}; (bottom row) Weighted Type I error indicators for c_{df}.

Analogous behaviour is also observed for the numerical approximation of the viscous stress induced drag coefficient, i.e., $J_{c_{\mathrm{df}}}(\mathbf{u})$. Indeed, from Table 2 we again see that the quality of the computed error representation formula is extremely
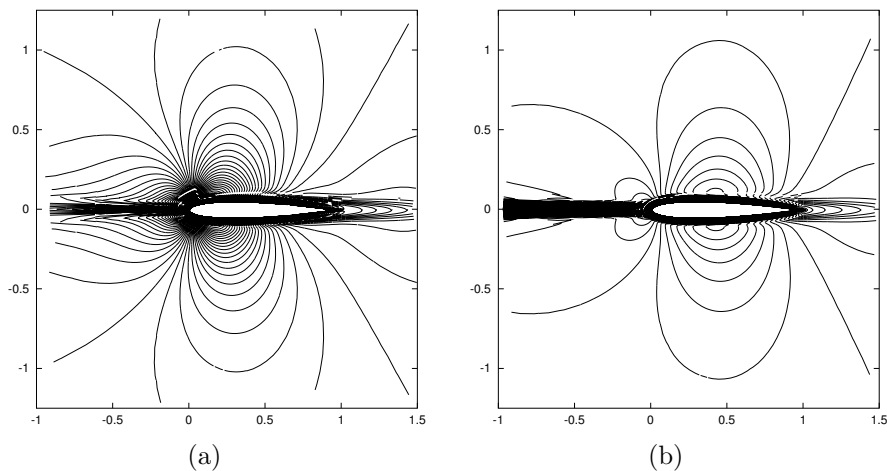
FIGURE 6. $M = 0.5, \mathrm{Re} = 5000, \alpha = 0°$ flow around the
NACA0012 airfoil: Isolines of component z_1 of the dual solution
for (a) c_{dp}; (b) c_{df}.

good as the mesh is refined; here, $\theta_1 \approx 1$ on the finer meshes. However, the loss
of sharpness of the Type I a posteriori error bound is now more pronounced; here,
θ_2 increases to a value of almost 33 on the finest mesh. In Figure 4, we compare
the true error in the computed functional $J_{c_{\mathrm{df}}}(\cdot)$ using the two mesh refinement
strategies, as well as the improved value of this target functional. As before, for
the computation of c_{dp}, we clearly see the superiority of employing the weighted
Type I error indicators in comparison with the Type II indicator: the former error
indicator leads to almost 2 orders of magnitude improvement in the error in the
computed viscous stress induced drag coefficient on the finest mesh. Indeed, we
note that the accuracy in the computed target functional on a mesh with only 8040
elements refined using the Type I indicator is still better than the accuracy on the
finest mesh with 34638 elements designed using the Type II indicator. Also, we
again note that the improved value of the target functional leads to a significant
reduction in the baseline error in the numerical approximation of c_{df}. Indeed, in
this case the error in the improved target functional $\tilde{J}_{c_{\mathrm{df}}}(\mathbf{u}_h)$ is over 2 orders of
magnitude smaller than the error in $J_{c_{\mathrm{df}}}(\mathbf{u}_h)$ computed on the sequence of meshes
generated by the weighted Type I error indicator.

Finally, in Figure 5 we show the meshes generated using both the Type II error
indicator $\eta_\kappa^{(\mathrm{II})}$, as well as the weighted Type I indicator for both the computation
of the pressure induced and viscous stress induced drag coefficients; note that since
$\eta_\kappa^{(\mathrm{II})}$ only depends on the dual solution through a global stability constant, the
same mesh is produced, irrespective of the choice of the target functional under
consideration. Here, we observe that the Type II error indicator mainly refines the
computational mesh in the region of the boundary layer, as well as in the long wake
behind the airfoil geometry. In contrast for both the computation of c_{dp} and c_{df},
we see that while the meshes generated by employing the weighted Type I error in-
dicator $\hat{\eta}_\kappa^{(\mathrm{I})}$ are both refined within the boundary layer, the wake is far less refined,
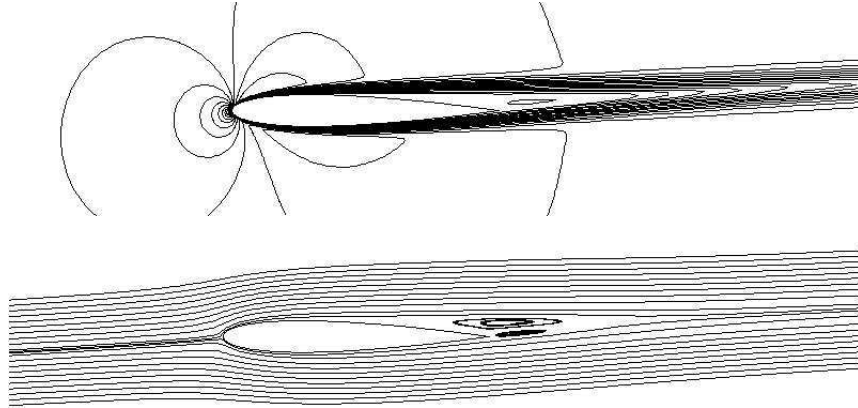
FIGURE 7. $M = 0.5, \mathrm{Re} = 5000, \alpha = 3°$ flow around the NACA0012 airfoil: (top) Mach isolines; (bottom) Streamlines.
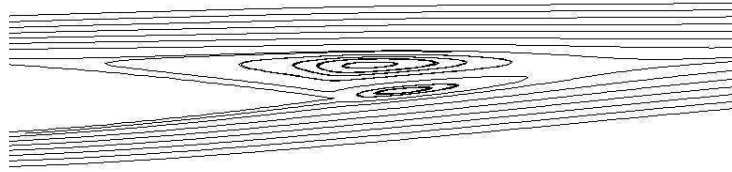

FIGURE 8. $M = 0.5, \mathrm{Re} = 5000, \alpha = 3°$ flow around the NACA0012 airfoil: Zoom of the streamlines at the trailing edge.

indicating that a good resolution of the wake is not important for the accurate computation of the pressure and stress induced drag coefficients, respectively. Indeed, from Figure 6, we see that while the corresponding dual solutions for c_{dp} and c_{df} exhibit boundary layers in the vicinity of the airfoil geometry, both dual solutions become increasing smooth as we enter the trailing edge wake. We also note that both dual solutions contain a strong singularity emanating from the leading edge of the airfoil; indeed, this leads to some additional refinement of the computational mesh directly in front of the airfoil geometry.

6.2. Mach 0.5 flow at Re = 5000 and $\alpha = 3°$ around a NACA0012. In this second example we again consider a laminar Mach 0.5 flow at $\mathrm{Re} = 5000$, but now prescribe an angle of attack of $\alpha = 3°$, in contrast to $\alpha = 0°$ which was employed in the previous example; cf. [20], for example. While the boundary layer in the previous example, see Figure 2, was completely attached to the surface of the airfoil geometry, the boundary layer in this example, see Figure 7, only remains attached on the lower surface; indeed, separation on the upper surface occurs at

Elements	DoF	$J(\mathbf{u}) - J(\mathbf{u}_h)$	$\sum_{\kappa \in \mathcal{T}_h} \hat{\eta}_\kappa$	θ_1	$\sum_{\kappa \in \mathcal{T}_h} |\hat{\eta}_\kappa|$	θ_2
3072	49152	-9.163e-02	-2.785e-02	0.30	3.549e-01	3.87
4950	79200	-1.713e-02	-1.649e-02	0.96	7.730e-02	4.51
7992	127872	-3.831e-03	-3.725e-03	0.97	1.741e-02	4.54
13194	211104	-1.035e-03	-1.022e-03	0.99	5.146e-03	4.97
21579	345264	-3.558e-04	-3.557e-04	1.00	2.424e-03	6.81

TABLE 3. $M = 0.5, \mathrm{Re} = 5000, \alpha = 3°$ flow around the NACA0012 airfoil: Adaptive algorithm for the numerical approximation of c_{lp} based on employing the Type I error indicator $\hat{\eta}_\kappa^{(\mathrm{I})}$.

Elements	DoF	$J(\mathbf{u}) - J(\mathbf{u}_h)$	$\sum_{\kappa \in \mathcal{T}_h} \hat{\eta}_\kappa$	θ_1	$\sum_{\kappa \in \mathcal{T}_h} |\hat{\eta}_\kappa|$	θ_2
3072	49152	8.486e-04	1.449e-03	1.71	6.877e-03	8.10
4983	79728	4.197e-04	4.611e-04	1.10	4.483e-03	10.68
8070	129120	2.390e-04	2.593e-04	1.08	2.384e-03	9.98
13266	212256	1.399e-04	1.436e-04	1.03	1.280e-03	9.15
21678	346848	7.742e-05	7.575e-05	0.98	6.590e-04	8.51

TABLE 4. $M = 0.5, \mathrm{Re} = 5000, \alpha = 3°$ flow around the NACA0012 airfoil: Adaptive algorithm for the numerical approximation of c_{lf} based on employing the Type I error indicator $\hat{\eta}_\kappa^{(\mathrm{I})}$.
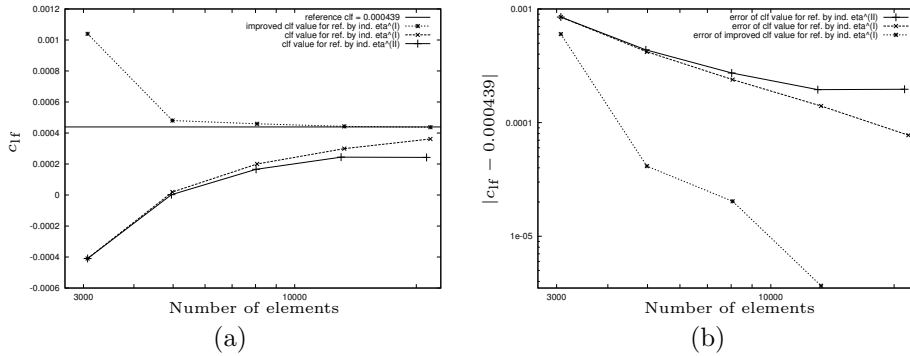

FIGURE 9. $M = 0.5, \mathrm{Re} = 5000, \alpha = 3°$ flow around the NACA0012 airfoil: (a) Computed values of c_{lf} based on employing the error indicators $\hat{\eta}_\kappa^{(\mathrm{I})}$ and $\eta_\kappa^{(\mathrm{II})}$, together with the improved value; (b) Convergence of the error in these quantities.

approximately 50% of the chord length, see Figure 8 for a close-up view of the separated flow. The force coefficients of the airfoil under these flow conditions strongly depend on the position of the flow separation and their numerical approximation represents a significantly more challenging task than for the previous example.

In contrast to the previous example, here we now consider the numerical approximation of the pressure induced and viscous stress induced lift coefficients, c_{lp} and
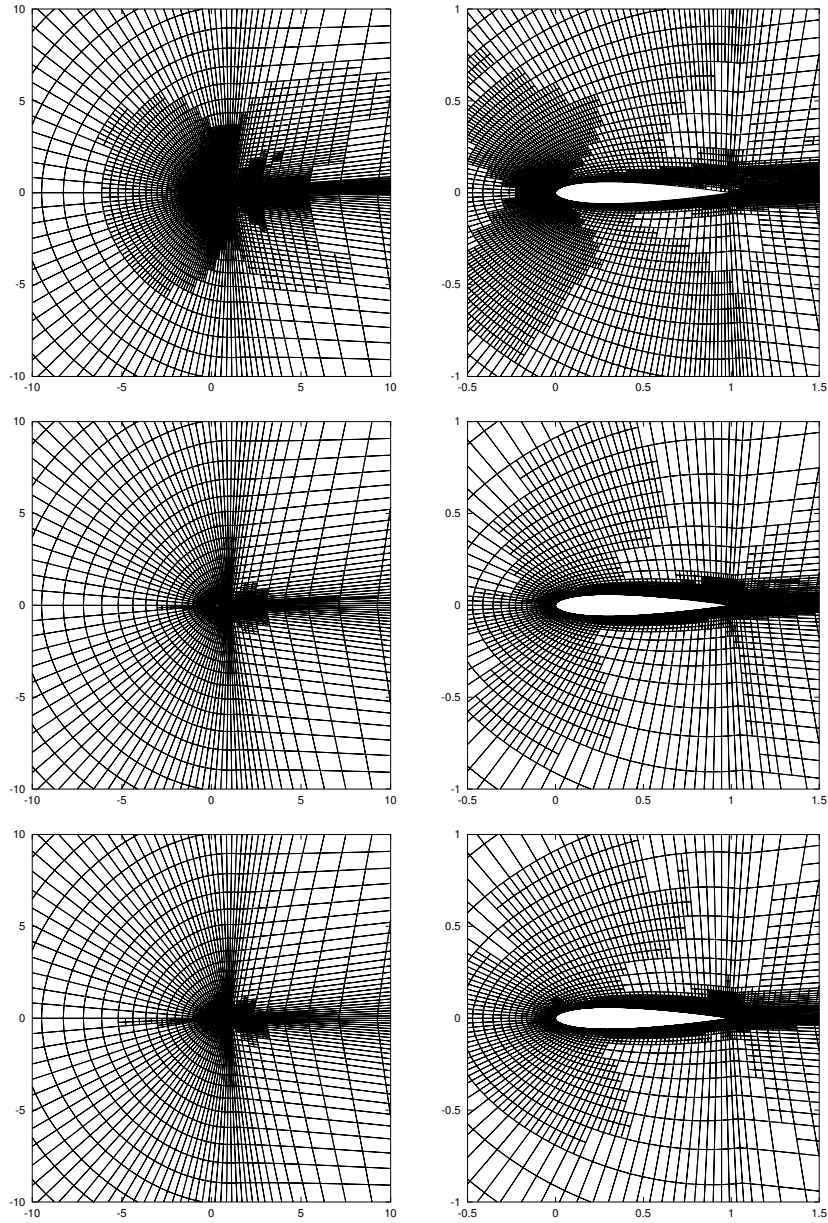
FIGURE 10. $M = 0.5, \mathrm{Re} = 5000, \alpha = 3°$ flow around the NACA0012 airfoil: Meshes constructed using (top row) Type II error indicators; (middle row) Weighted Type I error indicators for c_{lp}; (bottom row) Weighted Type I error indicators for c_{lf}.

c_{lf}, respectively. On the basis of a fine grid computation, the reference values for these target functionals are given by $J_{c_{\mathrm{lp}}}(\mathbf{u}) \approx 0.052524$ and $J_{c_{\mathrm{lf}}}(\mathbf{u}) \approx 4.39 \times 10^{-4}$. In Tables 3 and 4 we show the performance of our adaptive algorithm employing
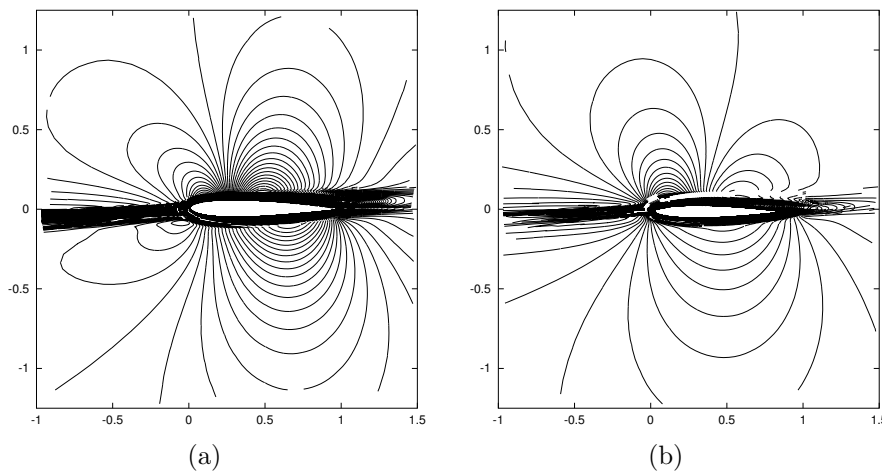
FIGURE 11. $M = 0.5, \mathrm{Re} = 5000, \alpha = 3°$ flow around the NACA0012 airfoil: Isolines of component z_1 of the dual solution for (a) c_{lp}; (b) c_{lf}.

the weighted Type I error indicator $\hat{\eta}_\kappa^{(\mathrm{I})}$, for both the numerical approximation of c_{lp} and c_{lf}, respectively. In each case we see that the quality of the computed error representation formula is extremely good; indeed, from the second mesh onwards the effectivity index θ_1 is extremely close to one. Moreover, the Type I a posteriori error bound provides a reliable upper bound on the true error in the computed target functional. In particular, while the effectivity index θ_2 slightly grows as the mesh is refined for the numerical approximation of c_{lp}, for c_{lf} we observe that θ_2 is relatively constant on each of the meshes employed.

In Figure 9 we present a comparison of the true error in the computed functional $J_{c_{\mathrm{lf}}}(\cdot)$ using the two mesh refinement strategies, as well as the improved value of this target functional. As in the previous example, we observe that the meshes designed by employing the weighted Type I error indicators lead to an improvement in the error in the computed target functional in comparison with the corresponding quantity computed on the sequence of meshes generated by the Type II error indicator $\eta_\kappa^{(\mathrm{II})}$. However, here the improvement is less dramatic than in the previous example; indeed, on the finest mesh we see that the error in the computed value of c_{lf} is only 3–4 times more accurate when $\hat{\eta}_\kappa^{(\mathrm{I})}$ is employed to design the mesh, as apposed to $\eta_\kappa^{(\mathrm{II})}$. However, for the latter error indicator, we observe that the error reduction from one mesh to the next is gradually becoming less as the mesh refinement algorithm proceeds, whereas, the weighed Type I error indicator leads to a constant reduction in $|J_{c_{\mathrm{lf}}}(\mathbf{u}) - J_{c_{\mathrm{lf}}}(\mathbf{u}_h)|$ as the mesh is refined. Finally, we again note that the improved value of target functional leads to a significant reduction in the baseline error. Analogous behaviour is also observed for the numerical approximation of c_{lp}; for brevity, we omit the results.

Finally, in Figure 10 we show the meshes generated using both the Type II error indicator $\eta_\kappa^{(\mathrm{II})}$, as well as the weighted Type I indicator for both the computation

of the pressure induced and viscous stress induced lift coefficients. As in the previous example, here we observe that the Type II error indicator mainly refines the computational mesh in the region of the boundary layer, as well as in the long wake behind the airfoil geometry. In contrast, for both the computation of c_{lp} and c_{lf}, we see that while the meshes generated by employing the weighted Type I error indicator $\hat{\eta}_\kappa^{(\text{I})}$ are both refined within the boundary layer, the wake is far less refined. Though, here we again observe some additional refinement of the mesh directly in front of the airfoil geometry, which corresponds to the region of the computational domain where the dual solutions exhibit a strong singularity emanating from the leading edge of the airfoil, cf. Figure 11.

7. Concluding Remarks

In this article, we have developed the a posteriori error analysis of the discontinuous Galerkin finite element method for the numerical approximation of the compressible Navier–Stokes equations in two–dimensional space. In particular, by employing a duality argument, we have derived (weighted) Type I and (unweighted) Type II a posteriori error bounds for general linear and nonlinear target functionals of the solution. Numerical experiments have been presented to illustrate the quality of the approximate error representation formula, when the (approximate) dual problem is approximated numerically. In particular, comparisons between Type I and Type II error indicators have clearly demonstrated the superiority of exploiting weighted a posteriori error indicators to guide adaptive mesh refinement. Moreover, provided the analytical solutions to the compressible Navier–Stokes equations and the corresponding dual problem are sufficiently smooth, then our numerical experiments also indicate that the computed approximate error representation may also be employed to improve the error in the computed value of the target functional under consideration.

Future extensions of this work include the consideration of three–dimensional compressible fluid flows, turbulent flows, anisotropic mesh refinement, as well as the simultaneous approximation of multiple target quantities of practical interest.

References

[1] D. ARNOLD, F. BREZZI, B. COCKBURN AND D. MARINI, *Unified analysis of discontinuous Galerkin methods for elliptic problems.* SIAM J. Numer. Anal. 39(5):1749–1779, 2002.

[2] W. Bangerth, R. Hartmann, and G. Kanschat. `deal.II` *Differential Equations Analysis Library, Technical Reference.* http://www.dealii.org/, 5.1 edition, Dec. 2004. first edition 1999.

[3] I. BABUŠKA AND M. SURI, *The hp–version of the finite element method with quasiuniform meshes*, M2AN Math. Model. Numer. Anal. 21:199–238, 1987.

[4] C.E. BAUMANN AND J.T. ODEN, *A discontinuous hp finite element method for the solution of the Euler and Navier–Stokes equations.* Int. J. Numer. Meth. Fluids 31:79–95, 1999.

[5] F. BASSI AND S. REBAY, *High–order accurate discontinuous finite element solution of the numerical solution of the compressible Navier–Stokes equations.* J. Comput. Phys. 131:267–279, 1997.

[6] R. BECKER AND R. RANNACHER, *An optimal control approach to a-posteriori error estimation in finite element methods.* In: Iserles, A. (ed), Acta Numerica, pp. 1–102, CUP, 2001.

[7] P.J. Capon, *Adaptive Stable Finite Element Methods for the Compressible Navier–Stokes Equations.* Ph.D. Thesis, University of Leeds, 1995.

[8] V. Dolejsi, *On the discontinuous Galerkin method for the numerical solution of the Euler and the Navier–Stokes equations.* Int. J. Numer. Methods Fluids, 45:1083–1106, 2004.

[9] M. Feistauer, J. Felcman and I. Straškraba, *Mathematical and Computational Methods for Compressible Flow.* Clarendon Press, Oxford, 2003.

[10] R. Hartmann. *Adaptive Finite Element Methods for the Compressible Euler Equations.* PhD thesis, University of Heidelberg, 2002.

[11] R. Hartmann *The role of the Jacobian in the adaptive discontinuous Galerkin method for the compressible Euler equations.* In G. Warnecke, editor, Analysis and Numerics for Conservation Laws, pp. 301–316, Springer, 2005. To appear.

[12] R. Hartmann and P. Houston, *Adaptive Discontinuous Galerkin Finite Element Methods for Nonlinear Hyperbolic Conservation Laws.* SIAM J. Sci. Comp., 24(3):979–1004, 2002.

[13] R. Hartmann and P. Houston, *Adaptive discontinuous Galerkin finite element methods for the compressible Euler equations.* J. Comp. Phys., 183:508–532, 2002.

[14] R. Hartmann and P. Houston, *Goal–oriented a posteriori error estimation for multiple target functionals.* In T.Y. Hou and E. Tadmor, editors, Hyperbolic Problems: Theory, Numerics, Applications, pp. 579–588, Springer-Verlag, 2003.

[15] R. Hartmann and P. Houston, *Adaptive discontinuous Galerkin finite element methods with interior penalty for the compressible Navier–Stokes equations.* In M. Feistauer, V. Dolejsi, P. Knobloch and K. Najzar, editors, Numerical Mathematics and Advanced Applications, ENUMATH 2003, pp. 410–419, Springer-Verlag, 2004.

[16] R. Hartmann and P. Houston, *Symmetric Interior Penalty DG Methods for the Compressible Navier–Stokes Equations I: Method formulation.* Int. J. Numer. Anal. Model., 2005. To appear.

[17] P. Houston, R. Hartmann and E. Süli, *Adaptive discontinuous Galerkin finite element methods for compressible fluid flows.* In M. Baines, editor, Numerical Methods for Fluid Dynamics VII, ICFD, pp. 347–353, 2001.

[18] M.G. Larson and T.J. Barth, *A posteriori error estimation for discontinuous Galerkin approximations of hyperbolic systems*, in Discontinuous Galerkin Methods, B. Cockburn, G. Karniadakis, and C.-W. Shu, eds., Lecture Notes in Comput. Sci. Engrg., 11, Springer, Berlin, 2000, pp. 363–368. .

[19] E. Süli and P. Houston, *Adaptive finite element approximation of hyperbolic problems.* In: Barth, T., Deconinck, H.(eds) Error Estimation and Adaptive Discretization Methods in Computational Fluid Dynamics. Lecture Notes in Computational Science and Engineering, Volume 25, pp. 269–344, Springer-Verlag, 2002.

[20] D. A. Venditti and D. L. Darmofal, *Anisotropic grid adaptation for functional outputs: application to two-dimensional flows.* J. Comp. Phys., 187:22–46, 2003.

Institute of Aerodynamics and Flow Technology, German Aerospace Center, Lilienthalplatz 7, 38108 Braunschweig, Germany.

E-mail: `Ralf.Hartmann@dlr.de`

School of Mathematical Sciences, University of Nottingham, University Park, Nottingham, NG7 2RD, UK.

E-mail: `Paul.Houston@nottingham.ac.uk`